Accepted Manuscript

Journal of
Materials Chemistry C

Materials for optical, magnetic and electronic devices
rsc.li/materials-c

Volume 6
Number 5
7 February 2018
Pages 911-1266

ISSN 2050-7526

ROYAL SOCIETY OF CHEMISTRY

PAPER
Nosang V. Myung, Yong-Ho Choe et al.
A noble gas sensor platform: linear dense assemblies of single-walled carbon nanotubes (LACNTs) in a multi-layered ceramic/metal electrode system (MLES)

This is an Accepted Manuscript, which has been through the Royal Society of Chemistry peer review process and has been accepted for publication.

Accepted Manuscripts are published online shortly after acceptance, before technical editing, formatting and proof reading. Using this free service, authors can make their results available to the community, in citable form, before we publish the edited article. We will replace this Accepted Manuscript with the edited and formatted Advance Article as soon as it is available.

You can find more information about Accepted Manuscripts in the Information for Authors.

ROYAL SOCIETY OF CHEMISTRY

rsc.li/materials-c

Brominated Trityl Radical Nanoparticles: Metal-Free Ratiometric Nanothermometer with Near-Infrared Excimeric Emission in Water

1
2
3

4 *Nerea Gonzalez-Pato,[1,2‡] Giovanni Schievano,[1‡] Pau Armada,[3] Jesús Cerdá,[4] Juan Aragó,[3] Jaume*

5 *Veciana,[1,2] Paula Mayorga-Burrezo,[1,2]* Imma Ratera[1,2]**

6

7 [1]Institute of Material Science of Barcelona (ICMAB-CSIC), Bellaterra, 08193, Spain.

8 [2]Networking Research Center on Bioengineering, Biomaterials and Nanomedicine (CIBER-

9 BBN), Bellaterra, 08193, Spain.

10 [3]Instituto de Ciencia Molecular (ICMol), Universitat de València, Catedrático José Beltrán 2,

11 Paterna 46980, Spain.

12 [4]Laboratory for Chemistry of Novel Materials, Université de Mons, Mons 7000, Belgium.

13

14 KEYWORDS. triarylmethyl radical, carbon centered organic radical, open-shell, fluorescence,

15 excimers, nanothermometry, NIR emission, organic nanoparticles

1

16

ABSTRACT

The development of efficient, metal-free luminescent nanothermometers operating near the first near-infrared (NIR-I) biological window is crucial for advancing biomedical imaging and temperature sensing at the nanoscale. In this work, we report a new family of brominated organic radical nanoparticles (**Br-ONPs**), prepared by nanoprecipitation of a persistent tris(2,4,6-tribromophenyl)methyl (TTBrM) radical doped into its optically inert precursor matrix (TTBrM-*αH*). Aqueous dispersions of **Br-ONPs** exhibit high colloidal stability, sizes below 130 nm, and dual emission under a single excitation. Thus, in addition to the emission of isolated monomeric TTBrM radicals inside the matrix, an excimeric band emerges at doping ratios ≥15 wt% due to simultaneous formation of TTBrM dimers with short intermolecular contacts inside the matrix which are similar to those present in crystalline polymorphs. Compared to chlorinated analogues (**Cl-ONPs**), **Br-ONPs** show the desired red-shift in both monomer and excimer emissions, entering into the interesting NIR-I window. Theoretical calculations support the electronic origin of the excimer emission and the role of bromine in modulating the optical properties. Temperature-dependent fluorescence studies confirm the suitability of metal-free **Br-ONPs** as a novel and efficient ratiometric nanothermometer in aqueous environments, with tunable optical output. Altogether, these findings not only establish **Br-ONPs** as promising candidates for future in vivo

34 bioimaging applications, but also provide valuable insights into the design principles and key

35 parameters governing the performance of organic nanothermometers.

36

Journal of Materials Chemistry C Accepted Manuscript

INTRODUCTION

As modern electronics grow increasingly compact and powerful, effective thermal management has become a key concern, with hot spots formation within device architectures jeopardizing their functionality and reducing their operational lifespan. This trend has driven strong interest in the design of efficient nanothermometers capable of sensing temperature variations within the submicrometric region and with optical outputs.[1,2] Nonetheless, not only the field of electronics is fuelling the progress in nanothermometry but also the field of biomedicine. Nanothermometry has also become a major technology for advancing biomedical research given that an accurate cellular temperature information is vital to fully understanding life science processes.[3,4] Promising performances of luminescent thermoresponsive nanoparticles (NPs) with precise temperature spatial and time resolution have been reported,[5] allowing the investigation of metabolic processes[6,7] or monitoring heat-based treatment in cancer therapy.[8] However, several limitations are hindering the broader application of light emission as a thermometric signal.[9]

Ratiometric luminescence systems have nevertheless emerged as reliable candidates for remote thermal mapping at the nanoscale, where conventional thermometers fail. Biological tissues, for instance, are not transparent and often exhibit autofluorescence in the visible range. Moreover, non-temperature related factors, such as the concentration of the dye or the excitation power dependence,[10] can also affect the performance of the emissive NPs. These constraints have underscored the value of ratiometric luminescence systems in overcoming such challenges.[10–13] Many examples of nanothermometers involving core shell metal organic particles with two dyes[14–16] or quantum dots[11,16] have appeared in the recent literature, describing their ability to provide

60 absolute measurements of temperature variations based on the ratio of fluorescence emission at

61 two different wavelengths. Nonetheless, it is worth noting that the rapid evolution of the field has

62 been mainly fuelled by lanthanide-based candidates owing to their ability to operate within the

63 near-infrared NIR-I (700–950 nm) and NIR-II (1000–1700 nm) biological windows,[17–23] where

64 reduced photon scattering and absorption processes enable an enhanced light penetration into

65 biological tissues. Despite their significant impact on nanothermometric imaging technologies,

66 lanthanide derivatives still pose possible concerns, including inconsistent *in vivo* toxicity and

67 unclear long-term safety profiles.[24–26] Alternatively, metal-free organic compounds, with easy

68 tuneable excitation and emission wavelengths, can significantly enhance biocompatibility too.

69 With such compounds, several strategies have been developed to construct organic ratiometric

70 nanothermometers suitable for aqueous environments. For instance, two organic fluorophores of

71 dissimilar thermoresponsiveness can be embedded in polymeric NPs that prevent their leakage.[27,28]

72 Another approach involves the use of temperature-sensitive polymeric matrixes undergoing phase

73 transitions to encapsulate stimuli-responsive organic emitters (*e.g.*, to molecular state of

74 aggregation,[29,30] or water presence[31]). Unfortunately, the phase transitions in the polymeric

75 matrixes usually occur in a narrow temperature interval which, in turns, produce an abrupt

76 modification of the fluorescent signal instead of progressive variation.

77 In recent studies within this area, some of us have demonstrated the potential of the stable

78 tris(2,4,6-trichlorophenyl)methyl radical (TTM) —a persistent halogenated triarylmethyls (trityl)

79 radical derivative— for application in ratiometric NIR-nanothermometry. Briefly, the TTM was

80 used as dopant within an optically neutral matrix made of its hydrogenated precursor, tris(2,4,6-

81   trichlorophenyl)methane (TTM-αH), to prepare a water suspension of nanoparticles by the re-

82   precipitation methodology.[32-34] The resulting aqueous dispersion of stable radical-based organic

83   nanoparticles (TTM-ONPs) exhibited an intrinsic dual emission thanks to the generation of an

84   excimeric emissive state in the region close to NIR at 567–665 nm, as a consequence of the

85   proximity of the radical neighbouring molecules within the ONPs.[32] The temperature dependence

86   of the excimeric emission in the TTM-ONPs favoured the development of a reliable, non-

87   cytotoxic, metal-free nanoscale temperature sensor,[32] which has been validated *in vivo*,[33] and under

88   two-photon excitation conditions in biological tissues.[34] Unfortunately, the emissions of TTM-

89   ONPs are still far from the NIR-I biological window thereby limiting some bioapplications. At this

90   point, it is important to stress that the above-mentioned properties are not generalizable to trityl

91   radicals, including many bearing different chlorinated shields. As a matter of example, the

92   formation of excimers was hindered when a fully chlorinated trityl derivatives, namely

93   perchlorotriphenylmethyl radical (PTM) and its non-radical precursor (PTM-*αH*), were used for

94   the ONPs preparation because its formation is controlled by subtle competing interactions.[32,34]

95   In this work, the nanostructuration of an alternative brominated trityl radical derivative will be

96   addressed. As depicted in **Scheme 1A**, the tris(2,4,6-tribromophenyl)methyl radical (TTBrM)[35]

97   will be combined with its optically neutral counterpart (TTBrM-*αH*) for the preparation of original

98   brominated ONPs (**Br-ONPs**). Despite the molecular functionalization of the *ortho-* and *para-*

99   positions with bulky bromine atoms, the generation of excimers is intended. In addition, the

100   TTBrM dopant concentration in **Br-ONPs** will be systematically optimized to enhance the dual

101   intrinsic emission under a single excitation wavelength (**Scheme 1B**). When compared with the

102   chlorinated TTM-ONPs, from now on **Cl-ONPs**, a redshift on the emissive properties is expected

103   for the **Br-ONPs** (**Scheme 1C**), as in the case of the emission spectra of the molecular radicals in

104   solution.[35] Thus, **Br-ONPs** are developed to enhance suitability for biomedical use, better meeting

105   the criteria required for applicability near the biological NIR-I transparency window. Theoretical

106   calculations will also be performed to address the impact of the brominated molecular shields on

107   the formation of excimeric states and the effect over the optical properties. Finally, the

108   performance of optimized **Br-ONPs** as ratiometric NIR-nanothermometers in aqueous media will

109   be tested (**Scheme 1D**).

110

111
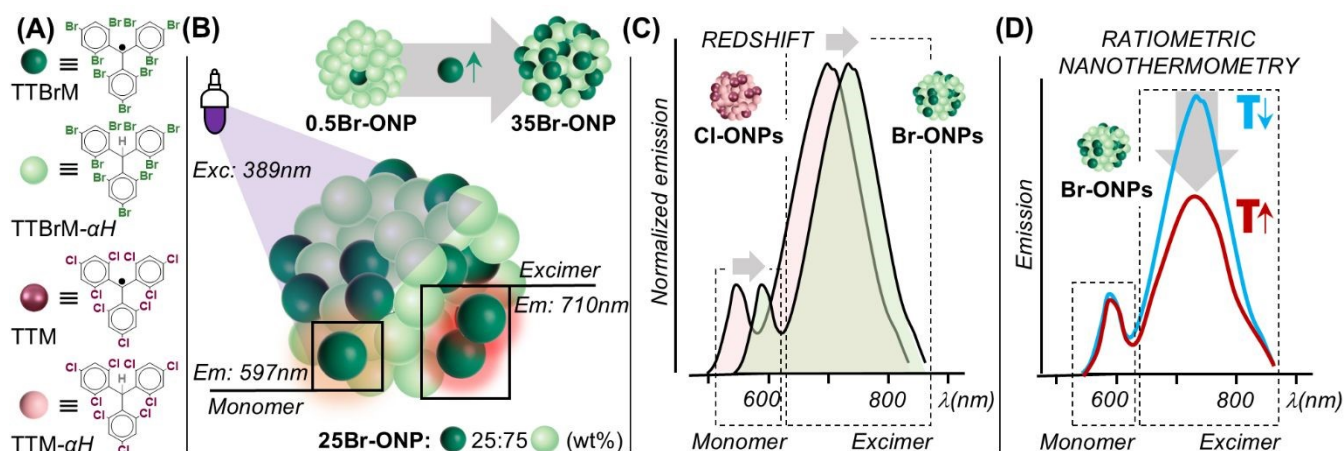
112   **Scheme 1. Ratiometric NIR-nanothermometer based on TTBrM radical.** Schematic representation

113   of: **(A)** the chemical structures of the open-shell TTBrM together with its non-radical precursor

114   (TTBrM-*αH*) and the chlorinated homologues TTM and TTM-*αH*, respectively; **(B)** the

115   brominated trityl radical-based organic nanoparticles (**Br-ONPs**) resulting from the combination

116   of TTBrM and TTBrM-*αH*. Increasing radical doping ratios, from 3 to 35 wt %, namely **3Br-ONPs**

117   to **35Br-ONPs**, have been explored aiming at the enhancement of the optical properties. The

118   presence of emissive monomer and excimers at higher radical doping ratios (*e.g.*, **25Br-ONPs**)

119   when irradiated with a single excitation wavelength has also been depicted; **(C)** comparison of the

120   fluorescence spectra of **Br-ONPs** and their homologues **Cl-ONPs**, highlighting the redshift

121   associated with the brominated molecular shields; **(D)** the temperature dependence of the

122   excimeric fluorescence band in optimized **Br-ONPs** and the derived ratiometric nanothermometric

123   functionality.

124   **RESULTS AND DISCUSSION**

125   Synthesis, crystal structure and organic nanoparticles (ONPs) preparation.

126   Tris(2,4,6-tribromophenyl)methane (TTBrM-*αH*) and tris(2,4,6-tribromophenyl)methyl radical

127   (TTBrM) were synthetized in line with previous reported procedures (see SI for further details).[35]

128   The obtained TTBrM was successfully crystallized, and two different polymorphs were identified.

129   One corresponds to a previously reported structure described by some of us, featuring platelet-like

130   crystals with a minimal C_{meta}–C_{meta} intermolecular distance of 4.092 Å between two neighbouring

131   radical molecules.[35] In addition, a new polymorph was discovered in the form of needle-shaped

132   crystals and exhibiting a shorter C_{meta}–C_{meta} distance of 3.802 Å (**Figure S2** and**S3** and **Table S1**

133   **and S2**). This value is comparable to that observed for TTM crystals (*i.e.,* 3.854 Å)[36] that is known

134   to form excimers when used to generate radical doped organic nanoparticles[33] (**Figure S3**). Both

135 polymorphs exhibit intermolecular distances shorter than those observed in the PTM crystals (*i.e.,*

136 4.237 Å), which do not form excimers when incorporated in their respective organic

137 nanoparticles.[34] This suggests that TTBrM, despite having a larger atomic radius, may also be

138 capable of forming excimers like TTM. Further structural details are provided in the SI.

139
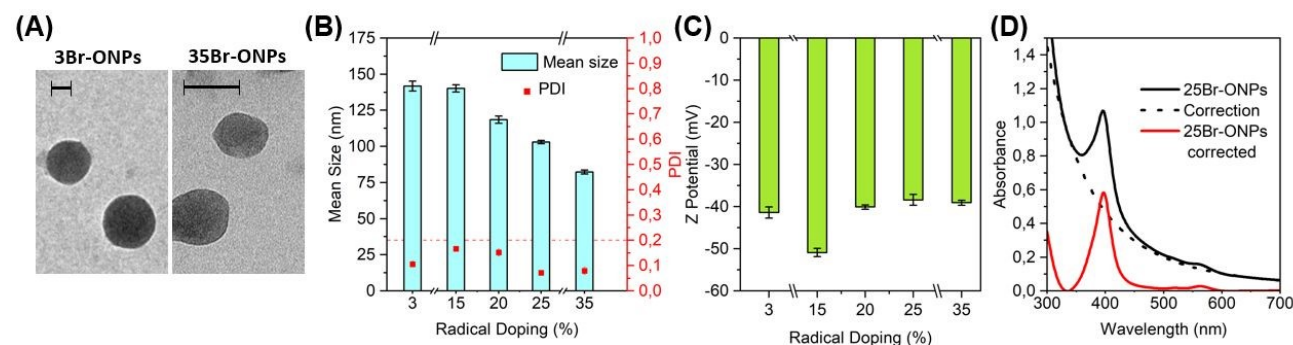
140 **Figure 1 Br-ONPs characterization. (A)** Representative TEM image of **3Br-ONPs** (left) and **35Br-**

141 **ONPs** (right). Scale = 50 nm in both cases; **(B)** hydrodynamic diameter evolution, polydispersity

142 (PDI) index and **(C)** *Z*-potential distribution with increasing TTBrM doping ratio of the **Br-ONPs**;

143 **(D)** UV--Vis electronic absorption spectra of **25Br-ONPs** water dispersion before (black) and after

144 (red) the mathematical treatment for scattering correction.

145

146   The preparation of the water suspension of **Br-ONPs** was done following the optimized re-

147 precipitation methodology reported for **Cl-ONPs** (See SI).[32–34] Given that pure emissive trityl

148 radicals exhibit a complete aggregation-caused quenching (ACQ) of fluorescence,[32] a

149 comprehensive library of aqueous suspensions of **Br-ONPs** was generated from the combination

150   of TTBrM and TTBrM-αH to gain further insights into their fluorescence behaviours. As in the

151   case of **Cl-ONPs**, the TTBrM-αH was chosen as a matrix for the ONPs because of: 1) its optically-

152   inactive behaviour in the range of absorption and emission of the TTBrM radical and also 2) the

153   similarities between the radical and non-radical molecular structures, providing good solvation,

154   preventing self-aggregation of the active radical and increasing the concentration quenching of the

155   luminescence. The radical content, or TTBrM doping ratio, was varied as follows: 3 wt% (**3Br-**

156   **ONPs**), 15 wt% (**15Br-ONPs**), 20 wt% (**20Br-ONPs**), 25 wt% (**25Br-ONPs**), and 35 wt% (**35Br-**

157   **ONPs**). Spherical-shaped ONPs were observed by transmission electron microscopy (TEM)

158   imaging for the resulting dispersions (**Figure 1A**).[32] Dynamic light scattering (DLS) measurements

159   showed sizes between 80 and 130 nm for all the **Br-ONPs** water colloidal dispersions and a

160   polydispersity index (PDI) below 0.2 for all of them, which is indicative of the high homogeneity

161   of the ONP suspensions. A modest decrease in the particle size is observed as the percentage of

162   radical doping inside the ONPs increase (**Figure 1B**). Moreover, a slightly average increase of

163   particle size of 7.5 % was observed across all dispersions after approximately 6 months (**Figure**

164   **S4**). In any case, all samples displayed negative surface potential values of around −40 mV (**Figure**

165   **1C**) ensuring very good colloidal stability. Electron paramagnetic resonance (EPR) measurements

166   were also conducted to gain further insight into the fate of the unpaired electrons in the radical

167   molecules. A successful transfer of the magnetic activity from the TTBrM to the water compatible

168   nanoassemblies was confirmed by the EPR signals recorded at room temperature from aqueous

169   **Br-ONPs** suspensions. As exemplified by the **20Br-ONPs** sample ($g = 2.0065$, **Figure S5**), g values
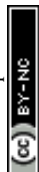
170   close to that of the free electron were observed in all cases. However, the significantly higher value

171   than the one reported for **Cl-ONPs** (*g*: 2.0030),[33] was attributed to the increased spin-orbit coupling

172   associated with the presence of the bromine atoms. As for the optical properties, a reported

173   mathematical treatment[37] was applied to correct the scattering of the UV-Vis electronic absorption

174   spectra of the **Br-ONP** suspensions in water (see, for instance, **25Br-ONPs** in **Figure 1D**). The

175   characteristic C band of trityl derivatives, attributed to delocalization of the unpaired electron

176   across the aromatic rings, was clearly observed at 389 nm, in line with the reported data for the

177   isolated molecule (**Figure S6B**).[35] In contrast, a red shift of 10 nm was detected when comparing

178   **20Br-ONPs** to analogous **20Cl-ONPs** (TTM-based ONPs with a radical content of 20% w/w,

179   **Figure S6A**). This experimental fact was attributed to the substitution of chlorine with bromine

180   atoms in the halogenated shields of both the radical and non-radical molecules comprising the

181   ONPs.

182

183   **Emissive properties of Br-ONPs: Excimer formation**

184   With the successful nanostructuration of TTBrM radicals into **Br-ONPs**, their fluorescence

185   behaviours were subsequently examined to complete their characterization. To this end, emission

186   spectra for each aqueous dispersion were recorded under a fixed wavelength excitation (λ_{exc} = 390

187   nm) at room temperature. As depicted in **Figure 2**, the spectra of **Br-ONPs** with low radical doping

188   ratios (*i.e.*, 3%) only showed a main emission band at 597 nm, in line with the fluorescence

189   spectrum of the isolated TTBrM in solution.[35] At such low concentration of TTBrM radical, the

190   molecules inside the **Br-ONPs** should be completely isolated, avoiding the aggregation-caused

191 quenching (ACQ) and also too far apart to electronically interact effectively, preventing the

192 formation of optically active excimers. A significant drop in the emission intensity of the monomer

193 contribution was observed for the ONPs with doping ratios above 15 %. With the increase of

194 radical doping, an additional band appear at longer wavelengths (*i.e.,* 710 nm), which is attributed

195 to the presence of excimeric species in line with the fluorescence spectra obtained for **Cl-ONPs**

196 under the same experimental conditions.[33] Thus, it was demonstrated that the bulkiness of the

197 brominated shield in TTBrM did not hinder the generation of excimeric species in **Br-ONPs** but

198 provoked an interesting red-shift in the overall emission spectrum, as noticed when compared with

199 the chlorinated counterpart (**20Cl-ONPs/Br-ONPs**: 567/597 nm and 665/710 nm, see **Figure S7**).

200 Both **Cl-ONPs** and **Br-ONPs** therefore reproduce the optical properties of the two molecules in

201 solution.[35] A comparison of the Fluorescence Quantum Yield (FQY) values of the two

202 formulations, the chlorinated and brominated ONPs, was also run, showing a similar trend to the

203 one reported for the isolated radicals in viscous organic solutions (see **Table S3**).[32,35] The less

204 electron-withdrawing nature of the Br atoms may account for the lower yield compared to TTM.

205 Finally, for high % of radical doping inside the **Br-ONPs** a quenching of fluorescence emission

206 was observed (see **Figure S8**). This effect was especially pronounced at doping ratios above 25 %,

207 in line with the expected ACQ of fluorescence when the radical molecules are not isolated. **Figure**

208 **S8A** shows the two competitive phenomena controlling the intensity of the fluorescence emission

209 of the **Br-ONPs** water suspension as the radical doping %; on one side, the excimeric emission

210 increases at 710 nm and, on the other side, the ACQ affecting the monomer emission, as well as

211 the excimeric emission in the case of radical dopings higher than 25%.

212

213
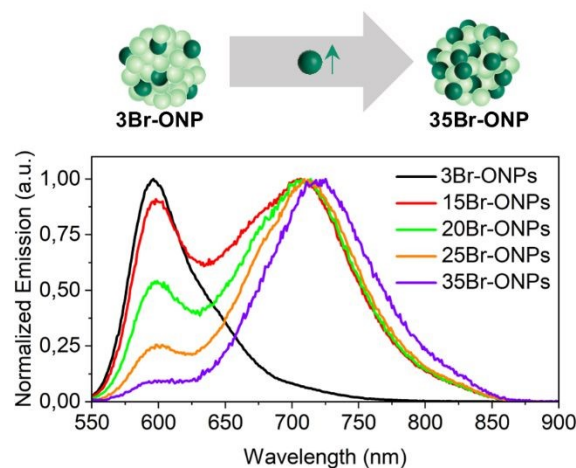
Figure 2. Fluorescence behaviour of Br-ONPs. Normalized emission spectra of **Br-ONPs** suspensions at different % of TTBrM content. Experimental details: all the water suspensions were measured at 20 ˚C and at a single excitation wavelength (λ_{exc}) at 390 nm.

217

To further understand the difference between the optical properties of both **Cl-** and **Br-ONPs**, a combined theoretical approach was employed, using electronic structure calculations, a powerful multistate diabatization scheme[38] and a model Hamiltonian to simulate the emission spectra of the monomer and dimer species of TTM and TTBrM (see SI for a detailed explanation). Briefly, the approach started with excited states calculations at the time-dependent density functional theory based on the crystal structures of the monomeric and dimer species of TTM and TTBrM (**Figure S13** and **Tables S7-S8**) to estimate the energy position of the relevant low-lying Frenkel (FE) and charge-transfer (CT) excited states. An optimally-tuned LC-ωhPBE functional ($\omega = 0.11$ bohr^{-1})[39–41] in combination with the 6-31G** basis set was employed for the excited state calculations,[42]

227 performed with the Gaussian 16 A.03 software package43 (see SI for additional details). Further

228 geometry optimizations of the FE- and CT-type excited states in monomer and/or dimer species of

229 TTM and TTBrM were also performed to estimate the adiabatic energies that are included in the

230 model Hamiltonian. This theoretical characterization is essential since the excimer formation in

231 molecular dimers requires a substantial mixing between FE and CT states along with a significant

232 structural relaxation (mostly due to intermolecular motions).[39–41] A brief analysis of the structural

233 changes for the optimized FE and CT states is given in SI (**Table S4** and **Figure S10**). The

234 electronic structure calculations were finally employed to parameterize the model Hamiltonian,

235 which is based on a Holstein−Peierls Hamiltonian that includes local and no local exciton-

236 vibrational couplings and electronic excitations of FE- and CT-type character. Note that this

237 vibronic Hamiltonian has been recently proposed by Spano and co-workers to successfully

238 describe the emission spectra in molecular excimers.[41,42]

239 **Figure 3A** shows a scheme of the important FE and CT excited (diabatic) states along with the

240 vibrational levels (close in energy) incorporated in the model Hamiltonian for the excimer

241 formation. **Figure 3B** compares the simulated emission spectra for the different species (monomer

242 or/and dimer) of TTM and TTBrM whereas **Figure 3C** displays the nature of the emissive vibronic

243 eigenstates. For TTBrM (**Figure 3B**), the simulated fluorescence spectrum for the monomer

244 exhibits an emission band with a distinguishable vibrational structure (peaked at 617, 664 and 720

245 nm) whereas the fluorescence spectrum for the dimer is significantly different with two well-

246 separated emission bands, a weak band predicted in the region of the monomeric radical (619 nm)

247 and a dominant broad and red-shifted emission band (701 nm) characteristic of the excimer
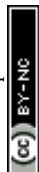
248 formation. The shape of the fluorescence spectra calculated for both the monomeric and dimer

249 species are in good agreement with those experimentally reported in **Figure 2** at the lowest and

250 highest radical doping ratio. Note that, at lowest radical doping ration, all the spectral signal come

251 from the radical monomer whereas, at the highest radical doping ration, the spectral signatures

252 would mainly arise from excimeric species (dimers). The theoretical findings therefore underpin

253 that, despite the bulkier size of bromine compared to chlorine, TTBrM can give rise to excimers

254 within the **Br-ONPs**. Likewise, the comparison of the simulated emission spectra for TTM and

255 TTBrM dimers clearly highlights that the excimeric emission for TTBrM is red-shifted compared

256 to TTM in line with the experimental evidences (**Figure S7**). This arises because the relevant FE

257 and CT excited states for TTBrM dimer are predicted at slightly lower energies than those found

258 for TTM (**Table S4**).

259

260
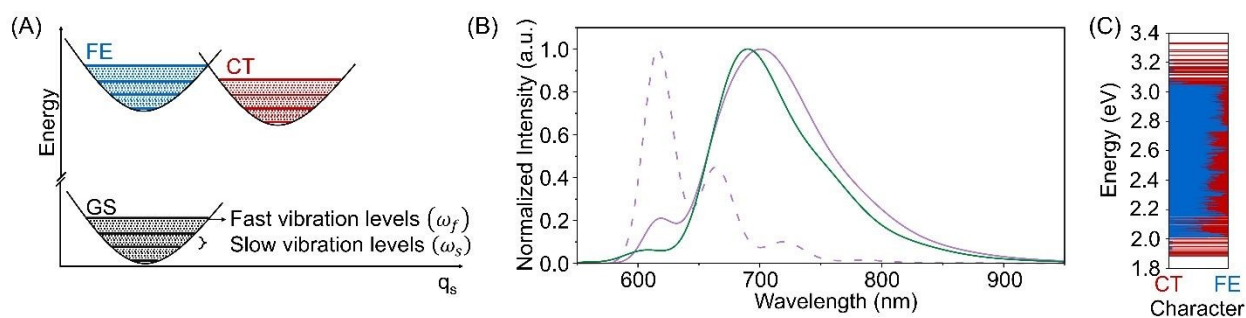
261 **Figure 3. (A)** Scheme of the relevant pure Frenkel (FE) and charge-transfer (CT) excited states

262 together with the vibrational levels involved for the excimer formation. **(B)** Comparison of the

263 simulated emission spectra for the TTBrM monomer (dotted purple), TTBrM dimer (purple) and

264 TTM dimer (green) at room temperature (20 °C). **(C)** Nature of the vibronic emitting eigenstates

265 (FE and CT character) for the TTBrM dimer.

266

267 **Thermometric performance of Br-ONPs**

268   The thermometric performance of **Br-ONPs** with different TTBrM radical doping % (**15Br-**

269 **ONPs**, **20Br-ONPs**, **25Br-ONPs** and **35Br-ONPs**) was investigated through temperature-

270 dependent emission measurements under 390 nm excitation (**Figure 4A** and **S9A–D**). All samples

271 display dual emission bands corresponding to the monomer (597 nm) and excimer (710 nm)

272 transitions. As the temperature increases from 5 °C to 55 °C, a gradual decrease in excimer

273 emission is observed across all samples, accompanied by a relatively stable or slightly increasing

274 monomer signal (**Figure S9E–H**), confirming a ratiometric thermometric response.

275   This behaviour correlated well with the simulated emission spectra of TTBrM dimers at different

276 temperatures (**Figure 4B**). As temperature increases, a decrease in the broad excimer band and a

277 slight increase in the monomer-like emission band were predicted, consistent with the thermal

278 population of the emissive vibronic states (**Figure S11**). At low temperatures, the dominant

279 emissive states exhibit a charge-transfer (CT) character with a slight FE-type contribution as

280 illustrated in **Figure 3C**. Although minor, this FE contribution is crucial as it endows these states

281 with optical activity (pure CT states typically lack significant oscillator strength and pure diabatic

282 FE vibronic states are the only ones that carry non-negligible oscillator strengths). At higher

283 temperatures, there is a tiny population transfer to vibronic states with a more FE-type nature

284 (monomer-like) and, consequently, the emission band intensities at the radical and excimer species

285 increase and decrease, respectively (**Figure 3, 4B** and **S11**), as observed experimentally.

286   To quantitatively describe this thermal behaviour, the luminescence intensity ratio (*LIR*) was

287   also calculated as $LIR = I_{Mon}/I_{Exc}$ across the entire temperature range, and fitted using the

288   empirical relation $LIR = a + b * e^{cT}$,[33,34,43] where I_{Mon} and I_{Exc} correspond to the emission

289   intensities of the monomer and the excimer, respectively (**Figure 4C** and **Figure S9I**). All systems

290   follow a sigmoidal trend, successfully fitted using **Equation 1**. In addition, the relative sensitivity

291   was calculated over the full temperature interval, using **Equation 1** (**Figure 4D** and **Figure S9K**).

292   The absolute sensitivity (S_a) (**Figure S9J**) reaches its maximum for **20Br-ONPs** but the relative

293   sensitivity (S_r), shown in **Figure S9K**, peaks for **25Br-ONPs** particularly considering their lower

294   signal variability, reinforcing their potential for biological applications. In terms of thermal

295   resolution, **25Br-ONPs** also display the lower temperature uncertainty (ΔT_{min}) among the series

296   (**Figure S9L**).

297

298
$$S_r = \frac{d(LIR)}{dT}\frac{1}{LIR} * 100\% \ [\% * K^{-1}]$$
         Equation 1

299

300   Altogether, these results highlight the strong influence of TTBrM content on thermometric

301   performance, with **25Br-ONPs** emerging as the optimal formulation based on multiple criteria:

302   higher luminescence intensity (before significant quenching), enhanced monomer-to-excimer

303   emission ration, high sensitivity, and excellent temperature resolution within the physiological

304   range (**Figure 4A**). It is worth noting that the sensitivity of **25Br-ONPs** remains consistently

305   between 1.8 and 2.3 % K^{-1} within the physiologic temperature range values well above the

306   commonly accepted threshold of 0.5 %K^{-1} for efficient nanothermometers.

307

308
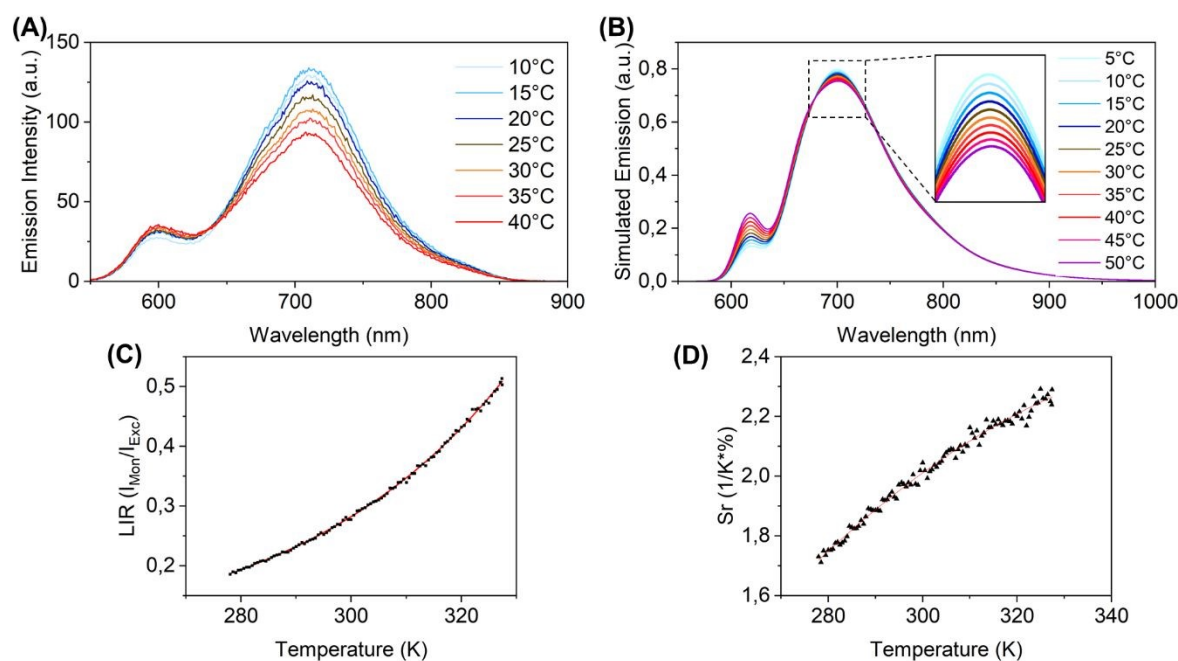
309   **Figure 4. Br-ONPs as ratiometric nanothermometers. (A)** Representative emission spectra of **25Br-**

310   **ONPs** at different temperatures, **(B)** Simulated emission spectra of TTBrM dimer as a function of

311   temperature, **(C)** LIR calculated (dots) and plotted (red line) between 5 and 55 °C and **(D)** relative

312   sensitivity calculated from individual points (dots) and from **Equation 1** (red line).

313

314   Same methodology was followed to test the thermometric properties of **20Cl-ONPs**, composed

315   of TTM radical, in previous works.[33,34] **Table 1** shows the differences in thermometric and optical

316   performances of the two metal-free radical-based nanoparticles. Compared with **20Cl-ONPs**,

317   **25Br-ONPs** are slightly less emissive without affecting significantly their optical-based

318   thermometric properties. The lost in emissive capacity can have its origin already at molecular

319   level since the oscillator strengths predicted for the first two excitations of the TTBrM radical are

320   slightly smaller than those obtained for the TTM radical (**Table S5**). Importantly, new **25Br-ONPs**

321   exhibit a red-shifted spectral profile, further extending their emission and entering into the first

322   biological transparency window, *i.e.* NIR-I region, which makes them particularly attractive for

323   *in-vivo* applications.

324

325   **Table 1.** Comparison of thermometric properties between **25Br-ONPs** and **20Cl-ONPs.**

Parameter	25Br-ONPs		20Cl-ONPs[33]	
Temperature	25 °C	37 °C	25 °C	37 °C
Monomer Emission	597 nm	597 nm	567 nm	567 nm
Excimer Emission	710 nm	710 nm	665 nm	665 nm
S_r (%K^{-1})	1.98	2.12	1.89	2.13
ΔT_{min} (K)	0.18	0.13	0.18	0.13

326   S_r: relative sensitivity; ΔT_{min}: minimum temperature interval detectable $\Delta T_{min} = \frac{\sigma(LIR)}{S_a} \, [K]$

327

328   CONCLUSIONS

329   In this work, we report the successful development of brominated trityl radical-based organic

330   nanoparticles (**Br-ONPs**) as fully organic, ratiometric nanothermometers operating in the near-

331   infrared region. By nanostructuring the TTBrM radical with its optically neutral and non-radical

332   precursor, TTBrM-*αH*, we achieved water-dispersed ONPs exhibiting dual emission from

333   monomeric and excimeric states under a single excitation wavelength. A systematic variation of

334   the radical content enabled the tuning of the emission properties, with excimer formation emerging

335   above 15 wt% doping. Compared to their chlorinated analogues (**Cl-ONPs**), **Br-ONPs** show red-

336   shifted emission, entering the NIR-I biological window, while retaining colloidal and

337   photophysical stability. Structural analyses revealed that, despite the increased bulkiness of

338   bromine atoms, intermolecular distances remained favourable for excimer formation, as supported

339   by crystallographic and spectroscopic data. Importantly, the excimer band in **Br-ONPs** exhibited

340   a temperature-dependent intensity, validating their applicability as ratiometric luminescent

341   nanothermometers in aqueous mediawith a nanothermometric sensitivity (S_r) of 1.8 - 2.3 % K^{-1}.

342   Therefore, these findings prove that **Br-ONPs** preserve the key advantages of trityl-based

343   nanothermometry, such as high photostability, ratiometric response, and water dispersibility, while

344   providing improved emission characteristics for biological imaging. Their fully organic

345   composition and red-shifted emission open new opportunities for the generation of robust,

346   biocompatible, and efficient temperature-sensing platforms for advanced biomaging and thermal

347   sensing applications in complex environments. Moreover, the rationalization of the theoretical

348   calculations implemented in this work will serve as a valuable tool for the future design of

349   optimized thermometric nanoparticles for biological applications.

350

351   ASSOCIATED CONTENT

352   **Supporting Information**. Additional experimental data are available free of charge in a PDF file.

353   AUTHOR INFORMATION

354 **Corresponding Author**

355 I. Ratera, iratera@icmab.es.

356 P. Mayorga-Burrezo, pmayorga@icmab.es

357

358 **Author Contributions**

359 N.G.-P. and G.S carried out all the activities related to the synthesis and characterization of the

360 ONPs. P. A., J. C. and J. A. where in charge of the theoretical calculations. J.V and I.R originated

361 the idea and P.M.-B. and I.R. supervised the project. P.M.-B. and I.R wrote the manuscript with

362 inputs from the rest of the authors. All authors have given approval to the final version of the

363 manuscript.

364 ‡These authors contributed equally.

365

366 ACKNOWLEDGMENT

391

392   REFERENCES

393   1   M. A. Kurochkin, D. V Mamonova, V. A. Medvedev, E. Y. Kolesnikov and I. E.
394   Kolesnikov, *Nanotechnology*, 2024, **35**, 295501.

395   2   R. Qian, X. Gong, H. Xue, W. Lu, L. Zhu and Z. An, *ES Energy and Environment*, 2019,
396   **6**, 4–17.

397   3   C. W. Chung and G. S. Kaminski Schierle, *ChemBioChem*, 2021, **22**, 1546–1558.
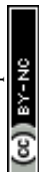
398 4   N. Yin, Y. Yu, X. Wang, Y. Shu and J. Wang, *Chemical Engineering Journal*, 2024, **490**,
399   151645.

400 5   B. del Rosal, E. Ximendes, U. Rocha and D. Jaque, *Adv Opt Mater*, 2017, **5**, 1600508.

401 6   N. Yin, B. Lin, F. Huo, Y. Shu and J. Wang, *Anal Chem*, 2022, **94**, 12111–12119.

402 7   Y. Takei, S. Arai, A. Murata, M. Takabayashi, K. Oyama, S. Ishiwata, S. Takeoka and M.
403   Suzuki, *ACS Nano*, 2014, **8**, 198–206.

404 8   R. Piñol, A. Millán, C. D. S. Brites, N. J. Silva and L. D. Carlos, in *Nanomaterials for
405   Magnetic and Optical Hyperthermia Applications*, Elsevier, 2019, pp. 139–172.

406 9   M. Quintanilla, M. Henriksen-Lacey, C. Renero-Lecuna and L. M. Liz-Marzán, *Chem Soc
407   Rev*, 2022, **51**, 4223–4242.

408 10   J. Zhou, B. del Rosal, D. Jaque, S. Uchiyama and D. Jin, *Nature Research*, 2020, preprint,
409   DOI: 10.1038/s41592-020-0957-y.

410 11   Y. Han, Y. Liu, H. Zhao, A. Vomiero and R. Li, *J Mater Chem B*, 2021, **9**, 4111–4119.

411 12   Y. Wang, Q. Zhang, C. Yang and Z. Xia, *Advanced Materials*, 2024, **36**, 2401057.

412 13   M. Liu, J. Liang and F. Vetrone, *Acc Chem Res*, 2024, **57**, 2653–2664.

413 14   M. Peng, A. M. Kaczmarek and K. Van Hecke, *ACS Appl Mater Interfaces*, 2022, **14**,
414   14367–14379.

415 15   W. Cao, Y. Cui, Y. Yang and G. Qian, *ACS Mater Lett*, 2021, **3**, 1426–1432.

416 16   Y. Chen, C. Li, T. Yang, E. A. Ekimov, C. Bradac, S. T. Ha, M. Toth, I. Aharonovich and
417   T. T. Tran, *ACS Nano*, 2023, **17**, 2725–2736.

418 17   N. Jurga, M. Runowski and T. Grzyb, *J Mater Chem C Mater*, 2024, **12**, 12218–12248.

419 18   Y. Wu, F. Li, Y. Wu, H. Wang, L. Gu, J. Zhang, Y. Qi, L. Meng, N. Kong, Y. Chai, Q. Hu,
420   Z. Xing, W. Ren, F. Li and X. Zhu, *Nat Commun*, 2024, **15**, 2341.

421 19   M. Jia, X. Chen, R. Sun, D. Wu, X. Li, Z. Shi, G. Chen and C. Shan, *Nano Res*, 2023, **16**,
422   2949–2967.

423 20   A. Puccini, N. Liu and E. Hemmer, *Nanoscale*, 2024, **16**, 10975–10993.

424 21   D. Ananias, F. A. Almeida Paz, L. D. Carlos and J. Rocha, *Chemistry – A European Journal*,
425   2018, **24**, 11926–11935.

426 22   M. Tan, F. Li, N. Cao, H. Li, X. Wang, C. Zhang, D. Jaque and G. Chen, *Small*, 2020, **16**,
427   2004118.

428   23   M. Zhao, A. Sik, H. Zhang and F. Zhang, *Adv Opt Mater*, 2023, **11**, 2202039.

429   24   Y.-T. Lin, R.-X. Liu, G. Audira, M. E. Suryanto, M. J. M. Roldan, J.-S. Lee, T.-R. Ger and
430   C.-D. Hsiao, *Toxics*, 2022, **10**, 336.

431   25   S. Premcheska, A. G. Skirtach and A. M. Kaczmarek, *Adv Nanobiomed Res*, 2025, **5**,
432   2500003.

433   26   V. Gonzalez, D. A. L. Vignati, C. Leyval and L. Giamberini, *Elsevier Ltd*, 2014, preprint,
434   DOI: 10.1016/j.envint.2014.06.019.

435   27   V. Kalaparthi, B. Peng, S. A. M. A. Peerzade, S. Palantavida, B. Maloy, M. E. Dokukin and
436   I. Sokolov, *Nanoscale Adv*, 2021, **3**, 5090–5101.

437   28   Y. Wu, J. Liu, J. Ma, Y. Liu, Y. Wang and D. Wu, *ACS Appl Mater Interfaces*, 2016, **8**,
438   14396–14405.

439   29   L. Li, C. Zhang, L. Xu, C. Ye, S. Chen, X. Wang and Y. Song, *Angewandte Chemie*
440   *International Edition*, 2021, **60**, 26725–26733.

441   30   K. Xue, S. Huang, K. Wu, Z. Sun, H. Fu, C. Wang, C. Wang and C. Zhu,
442   DOI:10.1021/acs.analchem.4c01803.

443   31   C. Wang, X. Zhao, K. Wu, S. Lv and C. Zhu, *Biosensors (Basel)*, 2022, **12**, 702.

444   32   D. Blasi, D. M. Nikolaidou, F. Terenziani, I. Ratera and J. Veciana, *Physical Chemistry*
445   *Chemical Physics*, 2017, **19**, 9313–9319.

446   33   N. Gonzalez-Pato, D. Blasi, D. M. Nikolaidou, F. Bertocchi, J. Cerdá, F. Terenziani, N.
447   Ventosa, J. Aragó, A. Lapini, J. Veciana and I. Ratera, *Small Methods*, 2024, **8**, 2301060.

448   34   D. Blasi, N. Gonzalez-Pato, X. Rodriguez Rodriguez, I. Diez-Zabala, S. Y. Srinivasan, N.
449   Camarero, O. Esquivias, M. Roldán, J. Guasch, A. Laromaine, P. Gorostiza, J. Veciana and
450   I. Ratera, *Small*, DOI:10.1002/smll.202207806.

451   35   P. Mayorga-Burrezo, V. G. Jiménez, D. Blasi, T. Parella, I. Ratera, A. G. Campaña and J.
452   Veciana, *Chemistry – A European Journal*, 2020, **26**, 3776–3781.

453   36   O. Armet, J. Veciana, C. Rovira, J. Riera, J. Castaner, E. Molins, J. Rius, C. Miravitlles, S.
454   Olivella and J. Brichfeus, *J Phys Chem*, 1987, **91**, 5608–5616.

455   37   J. Z. Porterfield and A. Zlotnick, *Virology*, 2010, **407**, 281–288.

456   38   Y.-C. Wang, S. Feng, W. Liang and Y. Zhao, *J Phys Chem Lett*, 2021, **12**, 1032–1039.

457   39   T. Körzdörfer and J.-L. Brédas, *Acc Chem Res*, 2014, **47**, 3284–3291.

458   40   T. Stein, L. Kronik and R. Baer, *J Am Chem Soc*, 2009, **131**, 2818–2820.

459   41   T. M. Henderson, A. F. Izmaylov, G. Scalmani and G. E. Scuseria, *J Chem Phys*,
460   DOI:10.1063/1.3185673.

461   42   M. M. Francl, W. J. Pietro, W. J. Hehre, J. S. Binkley, M. S. Gordon, D. J. DeFrees and J.
462   A. Pople, *J Chem Phys*, 1982, **77**, 3654–665.

463   43   M. J.%; T. G. W.%; S. H. B.%; S. G. E.%; R. M. A.%; C. J. R.%; et al. Frisch, *Gaussian*
464   *16, Revision B.01*, Gaussian, Inc., 2016.

465   44   Y. J. Bae, D. Shimizu, J. D. Schultz, G. Kang, J. Zhou, G. C. Schatz, A. Osuka and M. R.
466   Wasielewski, *J Phys Chem A*, 2020, **124**, 8478–8487.

467   45   D. Casanova, *Int J Quantum Chem*, 2015, **115**, 442–452.

468   46   A. L. Bialas and F. C. Spano, *The Journal of Physical Chemistry C*, 2022, **126**, 4067–4081.

469   47   H. Haghshenas, A. Bialas and F. C. Spano, *The Journal of Physical Chemistry C*, 2025, **129**,
470   6397–6413.

471   48   M. Jia, Z. Sun, M. Zhang, H. Xu and Z. Fu, *Nanoscale*, 2020, **12**, 20776–20785.

472

Data availability statement

All relevant data, including physicochemical characterization, TEM images, DLS measurements, and emission and luminescence spectra, are provided in the article and its supplementary information files. Additional specific data supporting the findings of this study and data from previously published articles, are available from the corresponding author upon reasonable request.

The crystallographic data for the structure reported in this manuscript have been deposited at the Cambridge Crystallographic Data Centre (CCDC), under deposition number 2473686. These data can be obtained free of charge from the CCDC via www.ccdc.cam.ac.uk/structures.